A non-unit line protection method for MMC-HVDC grids based on the curvatures of backward traveling waves

Xie, Fan; Hao, Zhiguo; Ye, Dongmeng; Yang, Songhao; Li, Chuanxi; Dai, Guoan; Zhang, Baohui; Wang, Ting

DOI
10.1016/j.ijepes.2023.109373

Publication date
2023

Document Version
Final published version

Published in
International Journal of Electrical Power and Energy Systems

Citation (APA)
Xie, F., Hao, Z., Ye, D., Yang, S., Li, C., Dai, G., Zhang, B., & Wang, T. (2023). A non-unit line protection method for MMC-HVDC grids based on the curvatures of backward traveling waves. *International Journal of Electrical Power and Energy Systems*, *153*, Article 109373. https://doi.org/10.1016/j.ijepes.2023.109373

Electrical Power and Energy Systems 153 (2023) 109373

Contents lists available at ScienceDirect

International Journal of Electrical Power and Energy Systems

journal homepage: www.elsevier.com/locate/ijepes

A non-unit line protection method for MMC-HVDC grids based on the curvatures of backward traveling waves

Fan Xie [a,b], Zhiguo Hao [a], Dongmeng Ye [a], Songhao Yang [a], Chuanxi Li [c], Guoan Dai [c], Baohui Zhang [a], Ting Wang [d,*]

[a] *School of Electrical Engineering, Xi'an Jiaotong University, Xi'an 710049, China*
[b] *Faculty of Electrical Engineering, Mathematics and Computer Science, Delft University of Technology, Delft 2628 CD, The Netherlands*
[c] *XJ Electric Co., Ltd., Xuchang 461000, China*
[d] *School of Electrical and Electronic Engineering, Nanyang Technological University, Singapore 639798, Singapore*

ARTICLE INFO

Keywords:
HVDC grids
Modular multilevel converters
Non-unit protection
Curvatures
Traveling waves

ABSTRACT

The existing protection techniques for high-voltage direct-current (HVDC) grids suffer from several shortcomings such as high sampling frequency, poor robustness, and reliance on simulation for threshold setting. To solve these problems, this paper proposes a non-unit protection method for modular multilevel converter (MMC)-based HVDC grids using the curvatures of backward traveling waves. To this end, the propagation characteristics of traveling waves and the boundary characteristics of DC lines are first studied, then the analytical expressions of backward traveling waves are derived. Moreover, the curvatures of backward traveling waves are analyzed. On this basis, a non-unit protection method is proposed, including zone selection, disturbance identification, and pole selection. At last, with a protection platform and a real-time digital simulator (RTDS) platform of the MMC-HVDC grid, the accuracy and the robustness of the proposed protection method are verified. The results show that the protection method can correctly identify faults with different distances and resistance in 1 ms and has strong robustness against transition resistance, sampling frequency, boundary value, noise, system topology, and line parameters.

1. Introduction

An imperative transition to renewable energies is taking place, to reduce global carbon emissions. Yet the limited capacity of the conventional system constrains the utilization of renewable energies [1,2]. In this regard, modular multilevel converter (MMC) based high-voltage direct-current (HVDC) technology has been proven to be one of the most promising solutions, due to its merits of no commutation failure, independent active and reactive power control, isolated islands power support, and multi-terminal grid construction [3,4].

MMC-HVDC grids use overhead lines to achieve long-distance transmission, in which the probability of fault is high [5]. The fault current develops very fast and exceeds the over-current withstand capacity of power electronic equipment within a few milliseconds, due to the low-inertia feature of MMC-HVDC grids [6]. Therefore, a protection device that can accurately identify faults and issue trip commands within 1–2 ms is needed [7].

The existing research works on the protection of MMC-HVDC grids can be categorized into three types, which are respectively based on artificial intelligence (AI) algorithms, frequency-domain characteristics of electrical quantities, and time-domain characteristics of electrical quantities [8].

The protection methods based on AI identify faults with pre-trained models, avoiding detailed explanations for complicated fault characteristics. AI methods, such as neural networks [9], support vector machines [10], stack auto-encoders [11], and genetic algorithms [12], are capable of classifying events under multiple impact factors. However, these methods are deficient in terms of interpretability and applicability. Furthermore, massive training data are acquired based on numerical simulations. Hence, these methods are still in the scientific research stage [13].

The protection methods based on frequency-domain characteristics rely on the boundary components of DC lines, such as filter capacitors and smoothing reactors. Fourier transform, wavelet transform [14], and empirical mode decomposition [15] are used to extract the energy distribution of different frequency bands. These methods can achieve

---

* Corresponding author.
E-mail address: wang.ting@ntu.edu.sg (T. Wang).

https://doi.org/10.1016/j.ijepes.2023.109373
Received 13 November 2022; Received in revised form 15 June 2023; Accepted 11 July 2023

frequency decomposition of signals with excellent time locality [16]. Yet, they require high sampling frequency [17], complicated calculation, and are susceptible to high-frequency disturbances and noises [18].

The protection methods based on time-domain characteristics primarily utilize the numerical characteristics of fault traveling waves such as change rates [19], ratios [20], variations [21], and integrations [22]. Besides, waveform characteristics, such as correlation [23] and direction [24], are also used. These variables are suitable for industrial applications, because their physical meanings are clear, and the calculation is simple. However, their threshold settings are highly dependent on simulations [13], and the sensitivity is insufficient in the cases of high resistance faults, which cause the malfunction of protection [18].

This work aims to develop a non-unit protection method for MMC-HVDC grids based on the curvatures of backward traveling waves, to make up for the shortcomings of the protection methods mentioned above. The propagation characteristics of traveling waves and the boundary characteristics of HVDC lines are first studied. On this basis, the analytical expressions of backward traveling waves are derived. Besides, the curvatures of backward traveling waves are analyzed, which are adopted to design a non-unit protection method. At last, the accuracy and the robustness of the protection method are verified with a protection platform and a real-time digital simulator (RTDS) platform of the Zhangbei MMC-HVDC grid.

The main contribution of this paper can be summarized as follows.

(1) This work derives the analytical expressions of the fault backward traveling waves for MMC-HVDC grids, based on which the threshold setting for protection can be determined beforehand without the need of simulation.
(2) This work innovatively proposes the curvatures of the voltage backward traveling waves as the protection criterion, and derives the analytical expressions of this feature under the internal and external faults.
(3) The impact factor analysis indicates that the protection method based on the curvatures of backward traveling waves has good sensitivity to high-resistance faults. The proposed protection method has been verified to withstand transition resistance up to 800 Ω.
(4) A protection platform is developed and tested with the RTDS platform. The test results show that the protection method can correctly identify faults of different types within 1 ms, and has sufficient robustness against sampling frequency, boundary value, noise, system topology, and line parameters.

The remainder of this paper is organized as follows. In Section 2, the basic theories of traveling waves are introduced. In Section 3, the analytical expressions of internal faults and external faults are derived for MMC-HVDC grids. In Section 4, the curvatures of backward traveling waves are further analyzed. In Section 5, a complete non-unit protection method based on curvatures is proposed. In Section 6, a hardware-in-the-loop (HIL) test system is built, and the verification and comparison are carried out.

2. Traveling waves theories

Traveling waves can accurately describe the fault transients in long-distance lines. When a fault occurs, fault voltage and current propagate from the fault location to both terminals in the form of traveling waves. The voltage $u(x,t)$ and the current $i(x,t)$ change with time and space, which can be expressed as the following superposition of traveling waves [23].

$$\begin{cases} u(x,t) = u_{\mathrm{f}}\left(t-\dfrac{x}{v}\right) + u_{\mathrm{b}}\left(t+\dfrac{x}{v}\right) \\ i(x,t) = \left[u_{\mathrm{f}}\left(t-\dfrac{x}{v}\right) - u_{\mathrm{b}}\left(t+\dfrac{x}{v}\right)\right] \Big/ Z_{\mathrm{C}} \end{cases} \tag{1}$$

where Z_{C} denotes the characteristic impedance, v denotes the wave velocity, u_{f} represents the voltage of forward traveling waves (FTWs), and u_{b} represents the voltage of backward traveling waves (BTWs). The direction from converter stations to lines is defined as the forward direction.

It is necessary to analyze the characteristics when traveling waves propagate in lines and pass through boundaries, to derive the analytical expressions of fault traveling waves.

2.1. Analysis of line propagation characteristics

When traveling waves propagate along transmission lines, time delays get generated, amplitudes get attenuated and waveforms get distorted. These effects can be expressed by the following line propagation function $A(s)$ in the complex frequency domain [8].

$$A(s) = \frac{1-kl}{1+s\cdot\tau l} e^{-s\cdot\frac{l}{v}} \tag{2}$$

where l denotes the transmission distance, the exponential term $e^{-sl/v}$ denotes the time delay, k denotes the amplitude attenuation effect per unit length, and τ denotes the waveform distortion effect per unit length.

2.2. Analysis of boundary characteristics

The refraction and the reflection of traveling waves occur at the boundary with discontinuous wave impedance, and the process is shown in Fig. 1. The mathematical relationships of the refracted waves $u_{\mathrm{f\ (B)}}(t)$, the reflected waves $u_{\mathrm{b\ (A)}}(t)$, and the incident waves $u_{\mathrm{f\ (A)}}(t)$ are as follows [25].

$$\begin{cases} U_{\mathrm{f\ (B)}}(s) = \dfrac{2Z_{\mathrm{B}}}{Z_{\mathrm{A}}+Z_{\mathrm{B}}} U_{\mathrm{f\ (A)}}(s) = \alpha U_{\mathrm{f\ (A)}}(s) \\ U_{\mathrm{b\ (A)}}(s) = \dfrac{Z_{\mathrm{B}}-Z_{\mathrm{A}}}{Z_{\mathrm{A}}+Z_{\mathrm{B}}} U_{\mathrm{f\ (A)}}(s) = \beta U_{\mathrm{f\ (A)}}(s) \end{cases} \tag{3}$$

2.3. Pole-mode transformation

The pole-to-pole and pole-to-ground mutual inductance can affect the transient characteristics of traveling waves. Pole-mode transformation is often used to decouple the mutual impacts [26], which can be expressed as,

$$\begin{bmatrix} U_{(1)} \\ U_{(0)} \end{bmatrix} = \boldsymbol{Q}\begin{bmatrix} U_{\mathrm{p}} \\ U_{\mathrm{n}} \end{bmatrix}, \begin{bmatrix} I_{(1)} \\ I_{(0)} \end{bmatrix} = \boldsymbol{Q}\begin{bmatrix} I_{\mathrm{p}} \\ I_{\mathrm{n}} \end{bmatrix}, \boldsymbol{Q} = \frac{1}{\sqrt{2}}\begin{bmatrix} 1 & -1 \\ 1 & 1 \end{bmatrix} \tag{4}$$

where U_{p} and U_{n} are the positive and the negative pole voltage, $U_{(1)}$ and $U_{(0)}$ are the 1-mode and the 0-mode voltage, I_{p}, I_{n}, $I_{(1)}$, and $I_{(0)}$ are defined similarly.

Compared with the 0-mode component, the 1-mode component takes polar lines as a path, and its loop parameters are not affected by the grounding situation. So the 1-mode component is more suitable for fault analysis, and it is also adopted in this work.

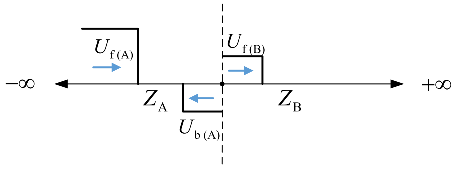

Fig. 1. Refraction and reflection of traveling waves.

3. Fault analysis for MMC-HVDC grids

This section is focused on the derivation of the expressions of fault traveling waves in the MMC-HVDC grid, whose main configuration is first introduced.

3.1. Main configuration of the MMC-HVDC grid

Zhangbei MMC-HVDC grid is adopted as the study case in this work, of which the primary part is shown in Fig. 2. The grid is a four-terminal symmetric bipolar system composed of half-bridge sub-module (HBSM) - MMCs. The four stations are connected via overhead transmission lines, which are connected to the busbar via current limiting reactors (CLRs) and DC circuit breakers (DCCBs). The DC line relay protection device (R) is located on the line side of CLRs. The rated DC voltage is ± 500 kV. Detailed parameters are provided in Section 6.1 [17].

F1, F2, F3, and F4 indicate representative fault locations in Fig. 2, taking relay protection $\mathrm{R_{MNp}}$ as the analysis object. F1 is the internal fault that occurs at the $\mathrm{Line_{MN}}$, F2 is the external fault that occurs at the DC Busbar N in the positive direction, F3 is the external fault that occurs at the adjacent $\mathrm{Line_{NQ}}$ in the positive direction, and F4 is the external fault that occurs in the opposite direction. The studied fault types include pole-to-ground (PTG) and pole-to-pole (PTP) faults. In addition, each fault can be a metallic fault or a high-resistance fault, according to transition resistance.

HBSM-MMCs and CLRs are located at both terminals of lines, and they can be represented with the equivalent impedance, forming the line boundaries of traveling waves. The dynamics of HBSM-MMCs can be ignored in the 1–2 ms data window for protection response. Therefore, MMCs can be simplified as the RLC series models [27]. Besides, the inductance of CLRs can be represented by L_{dc}.

For $\mathrm{R_{MNp}}$, the traveling waves generated by F1 are only affected by line propagation characteristics whereas the traveling waves generated by F2-F4 are affected by both line propagation characteristics and boundary characteristics.

3.2. Characteristic analysis for internal faults

To analyze fault traveling waves, their analytical expressions are first derived in the complex frequency domain, and then they will be transformed into time-domain expressions.

For $\mathrm{R_{MNp}}$, the first backward traveling waves in (1) show the initial fault characteristics, as they are not refracted or reflected by the local boundaries. All the backward traveling waves discussed in this paper refer to the initial ones.

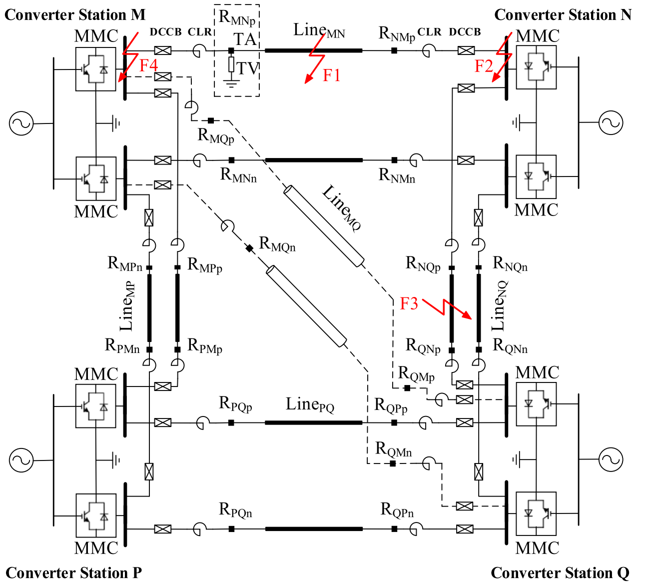

Fig. 2. Topology of Zhangbei MMC-HVDC grid.

Fig. 3 depicts the system model with F1. When F1 occurs, the 1-mode backward traveling waves $U_{\mathrm{b}(1)}(s)$ received by $\mathrm{R_{MNp}}$ can be expressed as,

$$U_{\mathrm{b}\,(1)}(s)=U_{\mathrm{F}\,(1)}(s)A(s)=\frac{u_{\mathrm{F}\,(1)}}{s}\frac{1-kl}{1+s\tau l}e^{-s\cdot\frac{l}{v_{(1)}}} \tag{5}$$

where $U_{\mathrm{F}(1)}(s)$ denotes the 1-mode fault traveling waves generated at the fault location, l denotes the fault distance, and $u_{\mathrm{F}\,(1)}$ denotes the amplitude of $U_{\mathrm{F}\,(1)}(s)$, which can be expressed as [25],

$$\begin{cases}\text{PTG fault:} & u_{\mathrm{F}\,(1)}=\dfrac{-\sqrt{2}Z_{\mathrm{C}(1)}U_{\mathrm{r}}}{Z_{\mathrm{C}(1)}+Z_{\mathrm{C}(0)}+4R_{\mathrm{f}}}\\[2ex] \text{PTP fault:} & u_{\mathrm{F}\,(1)}=\dfrac{-\sqrt{2}Z_{\mathrm{C}(1)}U_{\mathrm{r}}}{Z_{\mathrm{C}(1)}+R_{\mathrm{f}}}\end{cases} \tag{6}$$

where U_{r} denotes the rated voltage of DC lines and R_{f} denotes the transition resistance.

(5) can be rewritten as (7).

$$U_{\mathrm{b}(1)}(s)=A_0\ \left(\frac{1}{s}-\frac{1}{s+1/\tau_0}\right)e^{-s\cdot T_{\mathrm{d}}} \tag{7}$$

where

$$\begin{cases}A_0=u_{\mathrm{F}(1)}(1-kl)\\ \tau_0=\tau l\\ T_{\mathrm{d}}=l/v_{(1)}\end{cases} \tag{8}$$

And the time-domain expression of $U_{\mathrm{b}(1)}(s)$ can be obtained by inverse Laplace transform, as shown in (9).

$$u_{\mathrm{b}(1)}(t)=A_0\ \left(1-e^{-(t-T_{\mathrm{d}})/\tau_0}\right)\ \varepsilon(t-T_{\mathrm{d}}) \tag{9}$$

Equation (9) indicates that, when F1 occurs, $u_{\mathrm{b}(1)}(t)$ contains two parts: fault step waves and exponential waves caused by line propagation characteristics.

1-mode backward traveling waves $u_{\mathrm{b}(1)}(t)$ can be drawn according to (9). $u_{\mathrm{b}(1)}(t)$ (blue solid line) undergoes a rapid jump and observably deviates from the steady-state values, as shown in Fig. 4(a). Besides, the red dotted line indicates the 1-mode voltage traveling waves $u_{(1)}(t)$.

3.3. Characteristic analysis for external faults

3.3.1. External fault F2

When F2 occurs, $U_{\mathrm{F}(1)}$ will pass through the boundary (CLR) at the end of the line, as shown in Fig. 5(a). After voltage distribution, the waves $U^{'}_{\mathrm{F}(1)}$ propagate through the line and they will become the backward traveling waves $U_{\mathrm{b}(1)}$ measured by $\mathrm{R_{MNp}}$. $U_{\mathrm{b}(1)}$ can be expressed as,

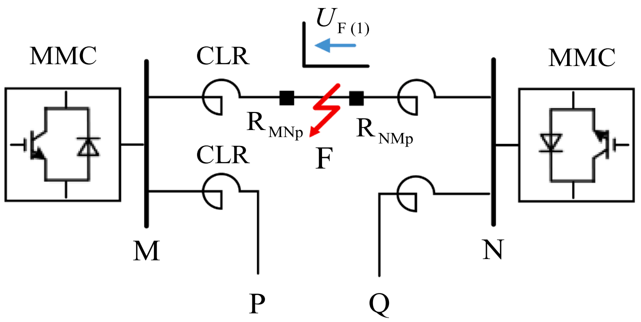

Fig. 3. System model with F1.

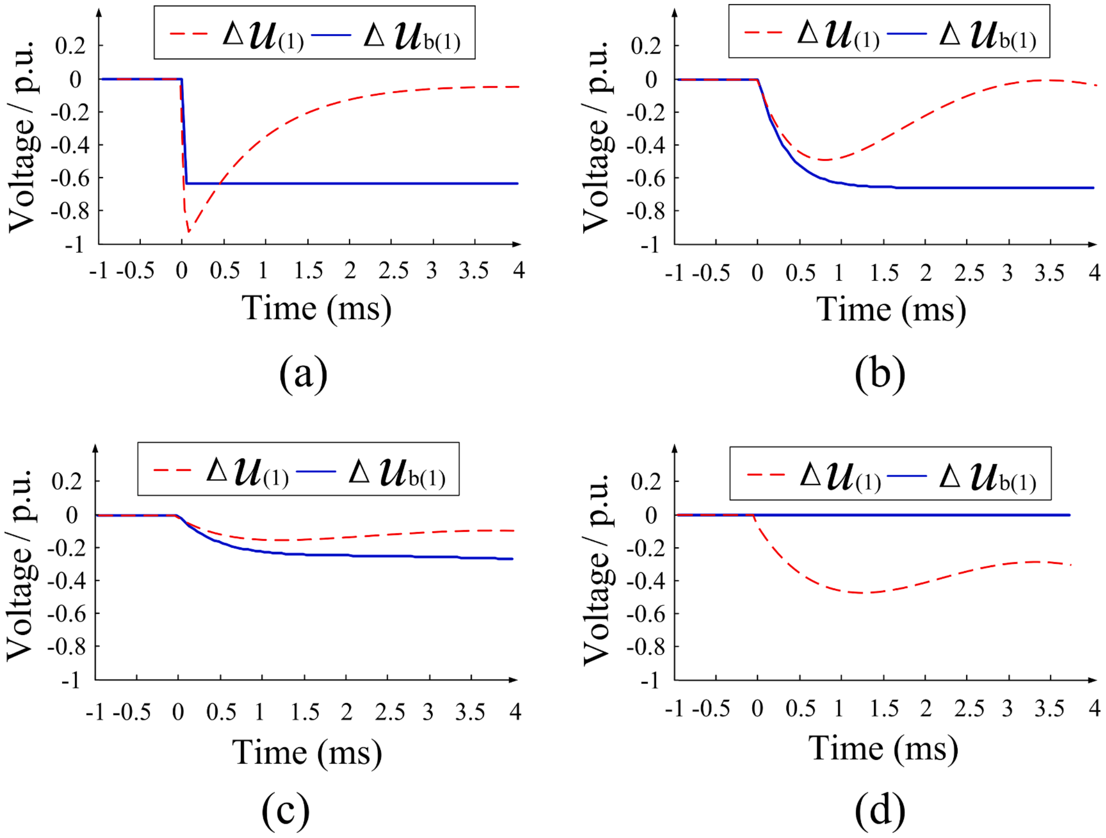

Fig. 4. Voltage traveling waves of different faults. (a) F1; (b) F2; (c) F3; (d) F4.

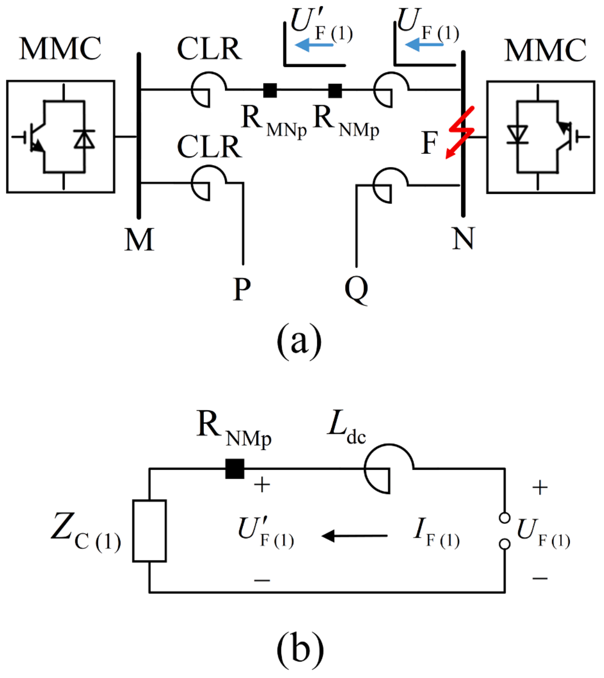

Fig. 5. System model and equivalent circuit with F2. (a) System model; (b) Equivalent circuit.

$$U_{b(1)}(s)=U'_{F(1)}(s)A(s)\quad=\frac{u_{F(1)}}{s}\frac{Z_{C(1)}}{sL_{dc}+Z_{C(1)}}\frac{1-kL}{1+s\tau L}e^{-s\cdot T_d} \tag{10}$$

where $U'_{F(1)}$ can be calculated from the equivalent circuit as shown in Fig. 5(b). $T_d=L/v_{(1)}$ and L is the full length of the line.

(10) can be rewritten as (11).

$$U_{b(1)}(s)=\left(\frac{A_1}{s}+\frac{A_2}{s+1/\tau_1}+\frac{A_3}{s+1/\tau_2}\right)e^{-s\cdot T_d} \tag{11}$$

where

$$\begin{cases} A_1=u_{F(1)}(1-kL) \\ A_2=u_{F(1)}(1-kL)\dfrac{L_{dc}}{Z_{C(1)}\tau L-L_{dc}} \\ A_3=u_{F(1)}(1-kL)\dfrac{Z_{C(1)}\tau L}{L_{dc}-Z_{C(1)}\tau L} \\ \tau_1=L_{dc}/Z_{C(1)} \\ \tau_2=\ \tau L \end{cases} \tag{12}$$

$u_{b(1)}(t)$ can be obtained by inverse Laplace transform, as shown in (13).

$$u_{b(1)}(t)=\left(A_1+A_2e^{-(t-T_d)/\tau_1}+A_3e^{-(t-T_d)/\tau_2}\right)\varepsilon(t-T_d) \tag{13}$$

Equation (13) indicates that when F2 occurs, $u_{b(1)}(t)$ is composed of three parts: the fault step waves, the exponential waves caused by boundary characteristics, and the exponential waves caused by line propagation characteristics.

The waveform of $u_{b(1)}(t)$ can be drawn according to (13). $u_{b(1)}(t)$ (blue solid line) drops smoothly, as shown in Fig. 4(b). Besides, the red dotted line indicates the 1-mode voltage.

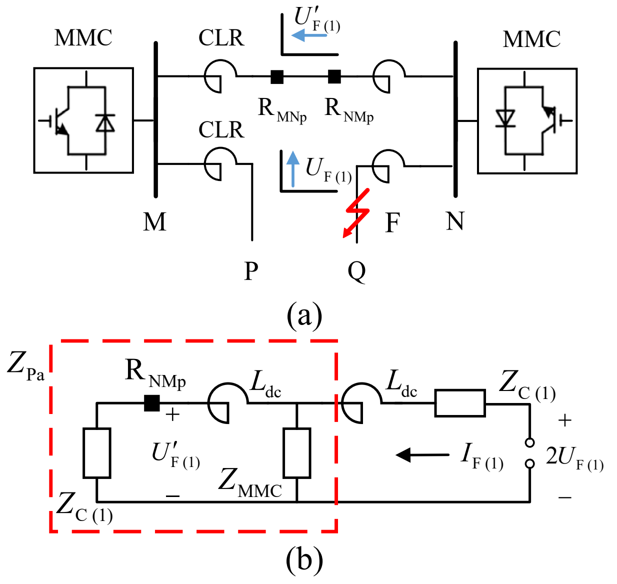

Fig. 6. System model and equivalent circuit with F3. (a) System model; (b) Equivalent circuit.

3.3.2. External fault F3

When F3 occurs, $U_{\mathrm{F(1)}}$ will pass through a more complex boundary than $U_{\mathrm{F(1)}}$ of F2, as Fig. 6(a) shows. After the refraction of waves $U_{\mathrm{F(1)}}$, the waves $U'_{\mathrm{F(1)}}$ propagate through the line and they will become the backward traveling waves $U_{\mathrm{b(1)}}$ measured by $\mathrm{R_{MNp}}$. $U_{\mathrm{b(1)}}$ can be expressed as,

$$\begin{aligned} U_{\mathrm{b(1)}}(s) &= U'_{\mathrm{F(1)}}(s)\ A_{\mathrm{L1}}(s)\ A_{\mathrm{L2}}(s) \\ &= \frac{u_{\mathrm{F(1)}}}{s}\frac{2Z_{\mathrm{C(1)}}}{sL_{\mathrm{dc}}+Z_{\mathrm{C(1)}}}\frac{Z_{\mathrm{Pa}}}{Z_{\mathrm{Pa}}+sL_{\mathrm{dc}}+Z_{\mathrm{C(1)}}}\frac{1-kL_1}{1+s\tau L_1}\frac{1-kL_2}{1+s\tau L_2}e^{-s\cdot T_{\mathrm{d}}} \end{aligned} \tag{14}$$

where $U'_{\mathrm{F(1)}}$ can be calculated from the equivalent circuit as shown in Fig. 6(b), which is drawn according to (3). $A_{\mathrm{L1}}(s)$ denotes the propagation function of the adjacent $\mathrm{Line_{NQ}}$, $A_{\mathrm{L2}}(s)$ denotes the propagation function of $\mathrm{Line_{MN}}$, L_1 and L_2 are the corresponding distances, $T_{\mathrm{d}} = (L_1+L_2)/v_{(1)}$, and Z_{Pa} is the parallel impedance, which can be expressed as,

$$Z_{\mathrm{Pa}} = (Z_{\mathrm{C(1)}}+sL_{\mathrm{dc}})\|Z_{\mathrm{MMC}} = (Z_{\mathrm{C(1)}}+sL_{\mathrm{dc}})\|\left(\frac{1}{sC_{\mathrm{eq}}}+sL_{\mathrm{eq}}+R_{\mathrm{eq}}\right) \tag{15}$$

where Z_{MMC} is the equivalent impedance of MMC, C_{eq} represents the sub-module capacitance in discharge, L_{eq} represents the bridge arm reactor L_{arm}, and R_{eq} represents the IGBT on-resistance $\sum R_{\mathrm{on}}$ and the arm resistance R_{arm}.

The detailed expression of the third term in (14) is as follows,

$$\begin{aligned} &\frac{Z_{\mathrm{Pa}}}{Z_{\mathrm{Pa}}+sL_{\mathrm{dc}}+Z_{\mathrm{C(1)}}} \\ &= \frac{L_{\mathrm{eq}}}{L_{\mathrm{dc}}+2L_{\mathrm{eq}}} + \frac{s\left[R_{\mathrm{eq}}C_{\mathrm{eq}} - \left(Z_{\mathrm{C(1)}}C_{\mathrm{eq}}+2R_{\mathrm{eq}}C_{\mathrm{eq}}\right)\left(\frac{L_{\mathrm{eq}}}{L_{\mathrm{dc}}+2L_{\mathrm{eq}}}\right)\right]}{s^2(L_{\mathrm{dc}}C_{\mathrm{eq}}+2L_{\mathrm{eq}}C_{\mathrm{eq}})+s(Z_{\mathrm{C(1)}}C_{\mathrm{eq}}+2R_{\mathrm{eq}}C_{\mathrm{eq}})+2} \\ &+\frac{1-\frac{2L_{\mathrm{eq}}}{L_{\mathrm{dc}}+2L_{\mathrm{eq}}}}{s^2(L_{\mathrm{dc}}C_{\mathrm{eq}}+2L_{\mathrm{eq}}C_{\mathrm{eq}})+s(Z_{\mathrm{C(1)}}C_{\mathrm{eq}}+2R_{\mathrm{eq}}C_{\mathrm{eq}})+2} \end{aligned} \tag{16}$$

According to the Veda theorem, it can be proved that the denominator of (16) has two different poles s_1 and s_2.

$$\begin{cases} s_1 = \dfrac{-Z_{\mathrm{C(1)}}C_{\mathrm{eq}}-2R_{\mathrm{eq}}C_{\mathrm{eq}}+\sqrt{\Delta}}{2\cdot(L_{\mathrm{dc}}C_{\mathrm{eq}}+2L_{\mathrm{eq}}C_{\mathrm{eq}})} \\ s_2 = \dfrac{-Z_{\mathrm{C(1)}}C_{\mathrm{eq}}-2R_{\mathrm{eq}}C_{\mathrm{eq}}-\sqrt{\Delta}}{2\cdot(L_{\mathrm{dc}}C_{\mathrm{eq}}+2L_{\mathrm{eq}}C_{\mathrm{eq}})} \end{cases} \tag{17}$$

$$\Delta = (Z_{\mathrm{C(1)}}C_{\mathrm{eq}}+2R_{\mathrm{eq}}C_{\mathrm{eq}})^2 - 8\cdot(L_{\mathrm{dc}}C_{\mathrm{eq}}+2L_{\mathrm{eq}}C_{\mathrm{eq}}) > 0$$

Therefore, (14) can be rewritten as (18).

$$U_{\mathrm{b(1)}}(s) = \left(\frac{A_1}{s}+\frac{A_2}{s+\frac{Z_{\mathrm{C(1)}}}{L_{\mathrm{dc}}}}+\frac{A_3}{s-s_1}+\frac{A_4}{s-s_2}+\frac{A_5}{s+\frac{1}{\tau L_1}}+\frac{A_6}{s+\frac{1}{\tau L_2}}\right)e^{-s\cdot T_{\mathrm{d}}} \tag{18}$$

where the constant $A_1 \sim A_6$ denote the amplitudes.

And $u_{\mathrm{b(1)}}(t)$ can be obtained by inverse Laplace transform, as shown in (19).

$$\begin{aligned} u_{\mathrm{b(1)}}(t) &= (A_1 + A_2e^{-\frac{Z_{\mathrm{C(1)}}}{L_{\mathrm{dc}}}(t-T_{\mathrm{d}})} + A_3e^{s_1(t-T_{\mathrm{d}})} + A_4e^{s_2(t-T_{\mathrm{d}})} \\ &+A_5e^{-\frac{1}{\tau L_1}(t-T_{\mathrm{d}})} + A_6e^{-\frac{1}{\tau L_2}(t-T_{\mathrm{d}})})\varepsilon(t-T_{\mathrm{d}}) \end{aligned} \tag{19}$$

The waveform of $u_{\mathrm{b(1)}}(t)$ can be drawn according to (19). $u_{\mathrm{b(1)}}(t)$ (blue solid line) drops more smoothly, as shown in Fig. 4(c). Besides, the red dotted line indicates the 1-mode voltage.

3.3.3. External fault F4

When F4 occurs, $U_{\mathrm{F(1)}}$ will pass through the boundary (CLR) at the beginning of the line, as Fig. 7 shows. After voltage distribution, the waves $U'_{\mathrm{F(1)}}$ propagate through the line as forward traveling waves (from converter stations to lines).

Hence, the backward traveling waves $U_{\mathrm{b(1)}}$ measured by $\mathrm{R_{MNp}}$ remain 0 until $U'_{\mathrm{F(1)}}$ is reflected by the end of the line, as shown in Fig. 4(d). Besides, the red dotted line indicates the 1-mode voltage, which deviates from the steady-state values.

3.3.4. Comparison between external faults

The worst-case scenario of external faults with the most obvious characteristics will be used for protection threshold setting. Since $u_{\mathrm{b(1)}}(t)$ of F4 remain 0, only F2 and F3 need to be compared.

To prove that F2 is a worse-case scenario than F3 under the same fault conditions, (10) and (14) are rewritten as (20).

$$\begin{cases} \text{F2:} \quad U_{\mathrm{b(1)}}(s) = c_{\mathrm{F2}}\dfrac{u_{\mathrm{F(1)}}}{s}\dfrac{1-kL}{1+s\tau L}e^{-s\cdot T_{\mathrm{d}}} \\ \text{F3:} \quad U_{\mathrm{b(1)}}(s) = c_{\mathrm{F3}}\dfrac{u_{\mathrm{F(1)}}}{s}\dfrac{1-kL_1}{1+s\tau L_1}\dfrac{1-kL_2}{1+s\tau L_2}e^{-s\cdot T_{\mathrm{d}}} \end{cases} \tag{20}$$

where c_{F2} and c_{F3} denote the scale factors.

c_{F2} is not less than c_{F3} in the frequency band presented, according to the analytical calculation shown in Fig. 8. Therefore, the absolute magnitude of $U_{\mathrm{b(1)}}$ is greater when F2 occurs, under the same fault conditions as F3.

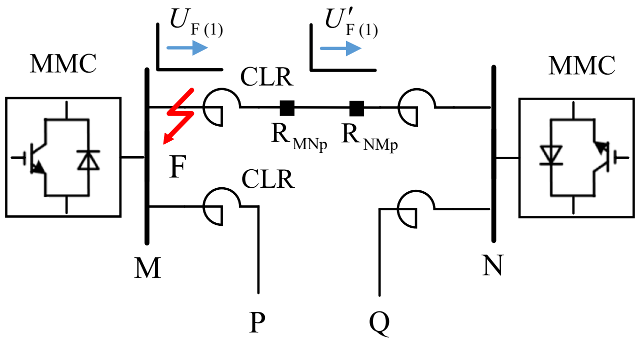

Fig. 7. System model with F4.

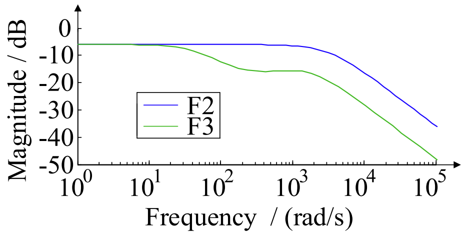

Fig. 8. Scale factors magnitude of F2 and F3.

4. Curvature analysis of backward traveling waves

The different characteristics of backward traveling waves caused by the faults at different locations can be described with the curvatures of $u_{\mathrm{b}(1)}(t)$. In the following discussion, the curvatures can not only avoid the dependence of threshold setting on simulation, but also maintain the sensitivity of protection under high-resistance faults.

4.1. Definition and calculation method of curvature

As shown in Fig. 9, the curvature κ is defined as follows [28].

$$\kappa = \lim_{\Delta\lambda\to 0}\left|\frac{\Delta\theta}{\Delta\lambda}\right| = \left|\frac{d\theta}{d\lambda}\right| \tag{21}$$

where θ denotes the angle that the curve tangent has turned and λ denotes the corresponding arc length.

In practice, if a curve can be represented by $y = f(t)$, its curvature κ can be calculated with (22) [28].

$$\kappa = \frac{|y^{''}|}{(1+y^{'2})^{\frac{3}{2}}} \tag{22}$$

where $y^{''}$ is the second derivative, $y^{'}$ is the first derivative.

4.2. Curvatures of internal faults

When F1 occurs, the analytical expressions of derivatives $u^{'}_{\mathrm{b}(1)}(t)$ and $u^{''}_{\mathrm{b}(1)}(t)$ are shown as (23), where$t^{'} = t - T_{\mathrm{d}}$.

$$\begin{cases} u^{'}_{\mathrm{b}(1)}(t) = A_0(1-e^{-\frac{t^{'}}{\tau_0}})\delta(t^{'}) + \dfrac{A_0}{\tau_0}e^{-\frac{t^{'}}{\tau_0}}\varepsilon(t^{'}) \\ u^{''}_{\mathrm{b}(1)}(t) = A_0(1-e^{-\frac{t^{'}}{\tau_0}})\delta^{'}(t^{'}) + \dfrac{2A_0}{\tau_0}e^{-\frac{t^{'}}{\tau_0}}\delta(t^{'}) - \dfrac{A_0}{\tau_0^2}e^{-\frac{t^{'}}{\tau_0}}\varepsilon(t^{'}) \end{cases} \tag{23}$$

The $\kappa_{\mathrm{b}(1)}$ of F1 can be calculated by (22) and (23). As shown in Fig. 10 (a), $\kappa_{\mathrm{b}(1)}$ is extremely high when F1 occurs and then rapidly drops to 0, corresponding to the sudden change and the constant steady-state value of $u_{\mathrm{b}(1)}(t)$ in Fig. 4(a).

4.3. Curvatures of external faults

F2 represents the worst-case scenario of external faults according to the amplitude of backward traveling waves $u_{\mathrm{b}(1)}(t)$, as analyzed in Section 3.3.4. When F2 occurs, the analytical expressions of $u^{'}_{\mathrm{b}(1)}(t)$ and $u^{''}_{\mathrm{b}(1)}(t)$ are represented by (24).

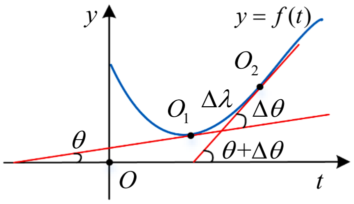

Fig. 9. Definition of curvature.

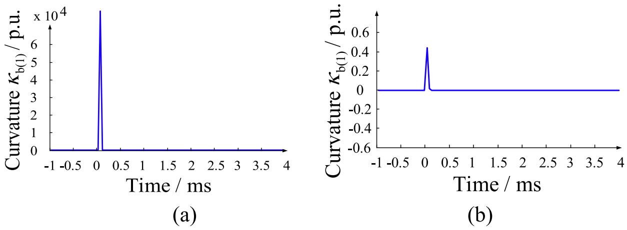

(a) (b)

Fig. 10. The curvatures of backward traveling waves during (a) F1, and (b) F2.

$$\begin{cases} u^{'}_{\mathrm{b}(1)}(t) & = (A_1 + A_2e^{-\frac{t^{'}}{\tau_1}} + A_3e^{-\frac{t^{'}}{\tau_2}})\delta(t^{'}) \\ & +(-\dfrac{A_2}{\tau_1}e^{-\frac{t^{'}}{\tau_1}} - \dfrac{A_3}{\tau_2}e^{-\frac{t^{'}}{\tau_2}})\varepsilon(t^{'}) \\ u^{''}_{\mathrm{b}(1)}(t) & = (A_1 + A_2e^{-\frac{t^{'}}{\tau_1}} + A_3e^{-\frac{t^{'}}{\tau_2}})\delta^{'}(t^{'}) + (-\dfrac{2A_2}{\tau_1}e^{-\frac{t^{'}}{\tau_1}} \\ & -\dfrac{2A_3}{\tau_2}e^{-\frac{t^{'}}{\tau_2}})\delta(t^{'}) + (\dfrac{A_2}{\tau_1^2}e^{-\frac{t^{'}}{\tau_1}} + \dfrac{A_3}{\tau_2^2}e^{-\frac{t^{'}}{\tau_2}})\varepsilon(t^{'}) \end{cases} \tag{24}$$

The $\kappa_{\mathrm{b}(1)}$ of F2 can be calculated by (22) and (24). As shown in Fig. 10 (b), $\kappa_{\mathrm{b}(1)}$ is small when F2 occurs and then drops to 0, corresponding to the smooth and continuous waveform of $u_{\mathrm{b}(1)}(t)$ in Fig. 4(b).

4.4. Impact factor analysis of curvatures

The traveling waves-based protection is activated by the arrival of fault traveling waves. Then, zone selection and pole selection must be completed within 1–2 ms after start-up [7]. To analyze the influencing factors on $u^{'}_{\mathrm{b}(1)}(t)$, $u^{''}_{\mathrm{b}(1)}(t)$ and $\kappa_{\mathrm{b}(1)}$ in this period, a quantitative analysis is carried out based on the line parameters given below: $Z_{\mathrm{C}(1)}$ is 320 Ω, $Z_{\mathrm{C}(0)}$ is 360 Ω, L_{dc} is 0.2 H, τ is 3×10^{-8} s/km, and k is 5×10^{-5} /km [5].

Besides, the following simplifications are made:

(1) The term corresponding to impulse function $\delta(t^{'})$ and $\delta^{'}(t^{'})$ are ignored in (23) and (24), since they only appear at the moment of fault occurrence ($t^{'} = 0$) and are not used for zone selection or pole selection.

(2) Since τ_1 (several ms)$\gg\tau_2$ (several μs), $e^{-t^{'}/\tau_2}$ decays faster than $e^{-t^{'}/\tau_1}$. So, $e^{-t^{'}/\tau_2}$ can be ignored in (24) during the period ($t^{'} \in (0, 1$ ms)) after $u_{\mathrm{b}(1)}$ arrives.

(3) Since $A_0/\tau_0\gg 1$ and $A_2/\tau_1\gg 1$ in (23) and (24), it can be proved that $\left|u^{'}_{\mathrm{b}(1)}\right|\gg 1$ during the period ($t^{'} \in (0, 1$ ms)). Hence, constant 1 can be ignored in the denominator of (22).

Based on the above simplifications, $\kappa_{\mathrm{b}(1)}$ of F1 and F2 can be rewritten as (25) and (26),

$$\kappa_{\mathrm{F1}}(t) = \frac{\left|-\frac{A_0}{\tau_0^2}e^{-t^{'}/\tau_0}\right|}{\left|\frac{A_0}{\tau_0}e^{-t^{'}/\tau_0}\right|^3}\varepsilon(t^{'}) = \left|\frac{\tau_0}{A_0^2}\right|e^{2t^{'}/\tau_0}\varepsilon(t^{'}) \tag{25}$$

$$\kappa_{\mathrm{F2}}(t) = \frac{\left|\frac{A_2}{\tau_1^2}e^{-t^{'}/\tau_1}\right|}{\left|-\frac{A_2}{\tau_1}e^{-t^{'}/\tau_1}\right|^3}\varepsilon(t^{'}) = \left|\frac{\tau_1}{A_2^2}\right|e^{2t^{'}/\tau_1}\varepsilon(t^{'}) \tag{26}$$

After (6), (8), and (12) are substituted into (25) and (26), $\kappa_{\mathrm{F1}}(t)$ and $\kappa_{\mathrm{F2}}(t)$ can be rewritten as,

$$\kappa_{\mathrm{F1}}(t) = \left|\frac{\left(Z_{\mathrm{C}(1)} + Z_{\mathrm{C}(0)} + 4R_{\mathrm{f}}\right)^2}{\left(-\sqrt{2}Z_{\mathrm{C}(1)}U_{\mathrm{r}}\right)^2}\frac{\tau l}{(1-kl)^2}\right|e^{\frac{2t^{'}}{\tau l}}\varepsilon(t^{'}) \tag{27}$$

$$\kappa_{\mathrm{F2}}(t)=\left|\frac{\left(Z_{\mathrm{C(1)}}+Z_{\mathrm{C(0)}}+4R_{\mathrm{f}}\right)^2}{\left(-\sqrt{2}Z_{\mathrm{C(1)}}U_{\mathrm{r}}\right)^2L_{\mathrm{dc}}Z_{\mathrm{C(1)}}}\frac{\left(Z_{\mathrm{C(1)}}\tau L-L_{\mathrm{dc}}\right)^2}{(1-kL)^2}\right|e^{\frac{2Z_{\mathrm{C(1)}}}{L_{\mathrm{dc}}}t'}\varepsilon(t') \tag{28}$$

According to (27) and (28), $\kappa_{\mathrm{F1}}(t)$ and $\kappa_{\mathrm{F2}}(t)$ are only related to fault distance l, line length L, and transition resistance R_{f}, when the line parameter Z_{C}, L_{dc}, τ, and k are fixed. On the one hand, $\kappa_{\mathrm{F1}}(t)$ and $\kappa_{\mathrm{F2}}(t)$ are positively correlated with R_{f} observably. On the other hand, by solving the derivatives of $\kappa_{\mathrm{F1}}(t)$ and $\kappa_{\mathrm{F2}}(t)$ with respect to l and$L$, it can be proved that $\kappa_{\mathrm{F1}}(t)$ is negatively correlated with l, and $\kappa_{\mathrm{F2}}(t)$ is negatively correlated with L. These two issues will be verified in Section 6.5.

The analysis indicates that when F2 occurs at the shortest distance with a high resistance, $\kappa_{\mathrm{F2}}(t)$ is the largest. This can be considered as the worst-case scenario of external faults, which will be used for threshold settings in Section 6.3.

5. Non-unit protection method based on the curvatures of backward traveling waves

To form a complete non-unit protection method, the criteria of zone selection, disturbance identification, and pole selection are studied as follows. All thresholds are set by analytical methods and are not dependent on simulation data.

5.1. Zone selection criterion

The magnitude difference of $\kappa_{\mathrm{b(1)}}$ can be represented by the positive or negative logarithm in different faults. The method uses $\lg\kappa_{\mathrm{b(1)}}$, and the criterion for internal faults is expressed as,

$$\lg\kappa_{\mathrm{b(1)}}\quad(k)\quad>\varepsilon_1 \tag{29}$$

where k is the sampling number and ε_1 denotes the threshold, whose setting principle is as follows.

$$\varepsilon_1=\ \mathrm{rel}_1\cdot\lg\ \kappa_{\mathrm{b(1)}\ \ (\max)} \tag{30}$$

where rel_1 denotes the reliability factor (set as 1.1–1.2) and $\lg\ \kappa_{\mathrm{b(1)(max)}}$ denotes the maximum logarithm value of $\kappa_{\mathrm{b(1)}}$ when external faults occur.

For the protection device, the calculation result of $u_{\mathrm{b(1)}}$ is discrete, and its derivatives can be approximated by the central difference formula shown in (31) [29]. Then, $\kappa_{\mathrm{b(1)}}$ can be calculated discretely after (31) is substituted into (22).

$$\begin{cases} u'_{\mathrm{b(1)}}(k)=\dfrac{u_{\mathrm{b(1)}}(k+1)\text{-}u_{\mathrm{b(1)}}(k\text{-}1)}{2T_{\mathrm{S}}} \\ u''_{\mathrm{b(1)}}(k)=\dfrac{u_{\mathrm{b(1)}}(k+1)\text{-}2u_{\mathrm{b(1)}}(k)+u_{\mathrm{b(1)}}(k\text{-}1)}{T_{\mathrm{S}}^2} \end{cases} \tag{31}$$

where T_{S} is the sampling interval.

5.2. Disturbance identification criterion

The voltage characteristic, adopted by the zone selection criterion, is easily affected by the disturbance due to lightning overvoltage or operation overvoltage. Therefore, it is necessary to identify the disturbances, to avoid the malfunction of protection.

The rise-fall-time ratio (RFTR) of 1-mode current is used for identifying lightning overvoltage disturbances, and the criterion for internal faults is expressed as [30],

$$RFTR(k)=\sum_{j=0}^{N-1}T_{\mathrm{rise}}(k-j)\Big/\sum_{j=0}^{N-1}T_{\mathrm{fall}}(k-j)>\varepsilon_2 \tag{32}$$

where T_{rise} denotes the rise time, T_{fall} denotes the fall time, and the calculation method is shown in (33). N is the number of integration points and ε_2 is the threshold, whose setting principle is shown as (34).

$$T_{\mathrm{rise}}(k)=\begin{cases}1, & \Delta i_{(1)}(k-1)<\Delta i_{(1)}(k)\\ 0, & \Delta i_{(1)}(k-1)\geqslant\Delta i_{(1)}(k)\end{cases} \tag{33}$$

$$T_{\mathrm{fall}}(k)=1-T_{\mathrm{rise}}(k)$$

where $\Delta i_{(1)}$ denotes the fault component of 1-mode current.

$$\varepsilon_2=\ \mathrm{rel}_2\cdot 1 \tag{34}$$

where rel_2 denotes the reliability factor (set as 1.1–1.2).

The fault component integration of 1-mode current before start-up is used to identify disturbances caused by DCCB operation overvoltage, and the criterion for internal faults is expressed as,

$$\mathrm{intg\_}i_{(1)}(k)=\left|\sum_{j=0}^{N-1}\Delta i_{(1)}(k-j)T_{\mathrm{S}}\right|<\varepsilon_3 \tag{35}$$

where $\mathrm{intg\_}i_{(1)}$ denotes the 1-mode current integration and ε_3 denotes the threshold, whose setting principle is expressed as,

$$\varepsilon_3=\ \mathrm{rel}_3\cdot\mathrm{intg\_}i_{(1)(\max)} \tag{36}$$

where rel_3 denotes the reliability factor (set as 0.8–0.85), and $\mathrm{intg\_}i_{1(\max)}$ denotes the maximum integration due to the current fluctuations during the steady state.

5.3. Pole selection criterion

The integration of 1-mode voltage and 0-mode voltage is used for pole selection, and the criterion is expressed as,

$$\begin{cases}\text{N - PTG fault: intg\_}u_{(0)}(k)>\varepsilon_4\\ \text{P - PTG fault: intg\_}u_{(0)}(k)<-\varepsilon_4\\ \text{PTP fault: }-\varepsilon_4\leqslant\mathrm{intg\_}u_{(0)}(k)\leqslant\varepsilon_4\ \&\&\mathrm{intg\_}u_{(1)}(k)<-\varepsilon_5\end{cases} \tag{37}$$

where $\mathrm{intg\_}u_{(1)}$ and $\mathrm{intg\_}u_{(0)}$ denote voltage integrations, whose calculation methods are shown as (38). ε_4 and ε_5 denote the thresholds, and their setting principles are shown as (39).

$$\begin{cases}\mathrm{intg\_}u_0(k)=\displaystyle\sum_{j=0}^{N-1}\Delta u_{(0)}(k-j)\ T_{\mathrm{S}}\\ \mathrm{intg\_}u_1(k)=\displaystyle\sum_{j=0}^{N-1}\Delta u_{(1)}(k-j)\ T_{\mathrm{S}}\end{cases} \tag{38}$$

where $\Delta u_{(1)}$ and $\Delta u_{(0)}$ denote the fault component of voltage.

$$\begin{cases}\varepsilon_4=\mathrm{rel}_4\cdot\mathrm{intg\_}u_{(0)(\max)}\\ \varepsilon_5=\mathrm{rel}_5\cdot\mathrm{intg\_}u_{(1)(\max)}\end{cases} \tag{39}$$

where rel_4 and rel_5 denote the reliability factor (set as 1.1–1.2), $\mathrm{intg\_}u_{(0)(\max)}$ and $\mathrm{intg\_}u_{(1)(\max)}$ denote the maximum integration due to voltage fluctuations during the steady state.

5.4. Non-unit protection method

The complete protection method is shown in Fig. 11, including the following steps.

1. The voltage and current in the mode domain are calculated according to (4), and the backward traveling waves $u_{\mathrm{b(1)}}$ in the mode domain are calculated according to (1);
2. The curvatures $\kappa_{\mathrm{b(1)}}$ are calculated according to (22) and (31), and internal faults are identified according to (29);
3. The *RFTRs* of 1-mode current are calculated and lightning overvoltage disturbances are identified according to (32–33);
4. The $\mathrm{intg\_}i_{(1)}$ are calculated and operation overvoltage disturbances are identified according to (35);
5. The $\mathrm{intg\_}u_{(1)}$ and $\mathrm{intg\_}u_{(0)}$ are calculated according to (38), and the faulty poles are identified according to (37);
6. Protection operates or protection resets.

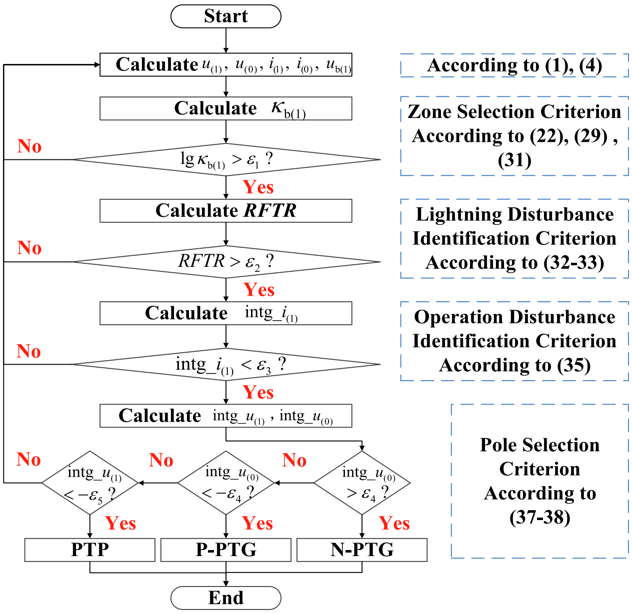

Fig. 11. Flow chart of the non-unit protection method.

6. Simulation and verification

6.1. HIL test system

A HIL test system consisting of an RTDS, an FPGA unit, an I/O interface, and a protection platform has been built with the support of XJ Electric CO., LTD., as shown in Fig. 12. The RTDS simulates the Zhangbei MMC-HVDC grid in Fig. 2, and it is used to generate simulation data on various faults and disturbances. The FPGA unit implements the detailed simulation of MMC, and the I/O interface enables the exchange of data between different devices. The protection platform is embedded with the proposed method, and it is tested in real time.

Four converter stations M, N, Q, and P in the grid all use HBSM-MMCs, and their rated DC voltages are all ± 500 kV. Line MN, NQ, QP, and PM are all overhead transmission lines, which use frequency-dependent models. And their lengths are 227 km, 126 km, 219 km, and 63 km. In addition, Line MQ is a 300-km-long cable line, which is added to verify the performance of the proposed method in different system topologies and line types. The initial sampling frequency is set to 20 kHz, the start time of each scenario is set to 0 ms, and the duration is set to 100 ms. Moreover, R_{MNp} is taken as the verification object, the fault scenarios have been described in Section 3.1, and the other detailed parameters are shown in Table 1 [17].

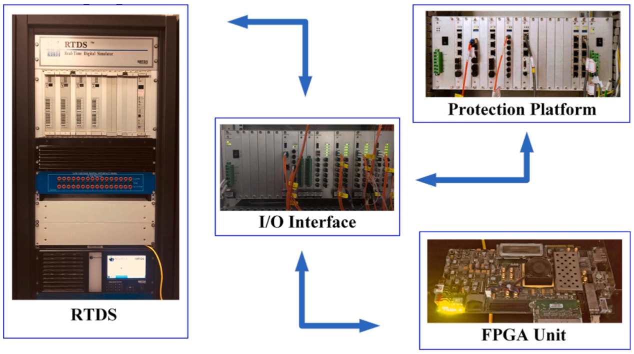

Fig. 12. The HIL test system.

Table 1
Parameters of Zhangbei MMC-HVDC grid.

Parameter	Station M	Station N	Station P	Station Q
Number of Sub-Modules	625	625	625	455
Sub-Modules Capacitor (mF)	10	10	10	15
Bridge Arm Reactor (mH)	80	80	80	80
Equivalent Resistance (Ω)	80	80	80	80
Current Limiting Reactor (mH)	200	200	200	200
Rated Power (MW)	3000	3000	1500	1500
Rated AC Voltage (kV)	220	220	500	500

6.2. Limit analysis of sampling frequency

According to (9) and (13), $u_{b(1)}$ of internal faults are step waves whereas $u_{b(1)}$ of external faults are the superposition of step waves and exponential waves, when ignoring the effect of line propagation characteristics. To obtain the continuous and smooth exponential waveforms of $u_{b(1)}$ during external faults, at least one point should be sampled during the decent process of the $u_{b(1)}$, so the maximum sampling interval $T_{s(max)}$ is half of the decent time T_{dec} [31].

As analyzed, $u_{b(1)}$ are the step responses of 1-mode fault traveling waves $u_{F(1)}$ generated at the fault location, and their T_{dec} can be defined as the time for dropping from 90 % to 10 % [32]. For an exponential wave $e^{-t/\tau}$, T_{dec} is m times the time constant τ, and according to the simplifications in Section 4.4, only τ_1 is used as the time constant τ when F2 occurs. The theoretical results of m and the minimum sampling frequency $F_{s(min)}$ are as follows.

$$m = \frac{t_{10\%} - t_{90\%}}{\tau_1} = \frac{(-\ln 0.1)\quad \tau_1 - (-\ln 0.9)\quad \tau_1}{\tau_1} = \ln 9 \tag{40}$$

where $t_{90\%}$ and $t_{10\%}$ are the time when e^{-t/τ_1} drops to 90 % and 10 %, respectively.

$$F_{s(min)} = \frac{1}{T_{s(max)}} = \frac{1}{T_{dec}/2} = \frac{2}{m \cdot \tau_1} = \frac{2 \cdot Z_{C(1)}}{\ln 9 \cdot L_{dc}} \approx 1.46 \quad \text{kHz} \tag{41}$$

where the values of $Z_{C(1)}$ and L_{dc} have been given in Section 4.4.

6.3. Threshold setting

The thresholds are set according to Section 5, and the setting results are shown in Table 2.

For ε_1 of protection R_{MNp}, the worst-case scenario of external faults is that F2 occurs at the shortest distance (Busbar N) with a high resistance (800 Ω), as analyzed in Section 4.4.

According to (22) and (24), $\lg\ \kappa_{b(1)(max)}$ can be analytically calculated in this scenario. The result is −1.30, which is always less than 0.

According to the operation requirements, the voltage and current fluctuation of each pole in the steady state shall be lower than 0.05p.u. [23]. Therefore, for ε_2, ε_3, ε_4, and ε_5, the maximum values of $\Delta i_{(1)}$, $\Delta u_{(1)}$ and $\Delta u_{(0)}$ are 0.071 p.u. according to (4). And the integration time in (32), (35) and (38) is set to 0.5 ms. Therefore, N is 10, and T_S is 0.05 ms

Table 2
Threshold setting.

Threshold	Reliability Factor	Parameter	Parameter Value	Threshold Value	Unit
ε_1	1.2	$\lg\kappa_{b(1)\ (max)}$	−1.30 (less than 0)	0	p.u.
ε_2	1.2	/	1	1.2	p.u.
ε_3	0.85	$\text{intg\_}i_{(1)\ (max)}$	0.036	0.031	p.u.·ms
ε_4	1.2	$\text{intg\_}u_{(0)\ (max)}$	0.036	0.043	p.u.·ms
ε_5	1.2	$\text{intg\_}u_{(1)\ (max)}$	0.036	0.043	p.u.·ms

(the initial sampling frequency is set to 20 kHz in Section 6.1).

For the protection method, 0.5 ms (t_1) data before and 0.5 ms (t_2) data after start-up are required. Besides, the sliding interval of the data window is 0.1 ms (t_3) and the signal processing time is 0.1 ms (t_4). To sum up, the total detection time (from fault traveling waves arriving at the protection device to the protection device outputting identification results) is 0.6 ms ($t_2 + t_4$).

6.4. Protection method verification

The PSCAD platform is also built with the same parameters described in Section 6.1. Simulations are carried out for different short-circuit faults (only metallic faults) and disturbances based on the RTDS platform and the PSCAD platform. The $u_{b(1)}$ of the representative scenarios are provided in Fig. 13 and the verification results of the protection method are shown in Table 3 and Table 4. The difference in the waveforms of the $u_{b(1)}$ is mainly caused by the different models of the power electronic devices on the two platforms: In RTDS, the MMCs and DCCBs are modeled using detailed equivalent models (DEMs), which can ensure the accuracy of the HIL tests [33], whereas an energy equipartition model (EEM) is used in PSCAD, due to the need to balance the efficiency and accuracy of the simulation [34]. This simplification improves the efficiency of the simulation, yet leads to the slightly different simulation results, as shown in Fig. 13. Nevertheless, this inconsistency in the simulation results is trivial for the curvature-based method, because only the amplitude of $u_{b(1)}$, rather than their waveform characteristics, are mainly affected.

6.4.1. Results and discussion of short-circuit faults

As shown in Fig. 13, when the metallic F1 with different l occur, the initial $u_{b(1)}$ are almost consistent, with a small difference caused by the line propagation characteristics. When metallic F2, F3, and F4 occur, the initial $u_{b(1)}$ are very smooth with lower amplitudes, compared with the $u_{b(1)}$ of F1. Besides, the $u_{b(1)}$ of F2 has the largest amplitude among the external faults, which has been analyzed in Section 3.3.4. In addition, when the fault parameters are the same, the amplitudes of the $u_{b(1)}$ of PTP faults are greater than the $u_{b(1)}$ of PTG faults, which can be proven by substituting the parameters into (6).

As shown in Table 3, the minimum $\lg\kappa_{b(1)}$ of F1 is 0.9545, which is more than ε_1, when a PTP fault occurs at the far end of Line$_{MN}$, and therefore the protection can be correctly triggered according to (29). And the $\lg\kappa_{b(1)}$ decreases when l increases, as analyzed in (27) and (28). Besides, the $\lg\kappa_{b(1)}$ of PTP faults are smaller than PTG faults with the same parameters, which are consistent with the derivation when substituting (6) into (25) and (26). The maximum $\lg\kappa_{b(1)}$ of external faults is -1.1118 when F2 occurs at Busbar N, which is much less than ε_1, and therefore the protection will not be mis-triggered.

For each scenario of F1, the *RFTR* is infinite and the maximum intg_$i_{(1)}$ (0.0196) is less than ε_3, hence, the criteria in (32) and (35) are satisfied. Furthermore, the intg_$u_{(0)}$ of each PTP fault is 0 and the maximum intg_$u_{(1)}$ (–0.6719) is less than $-\varepsilon_5$, while the maximum intg_$u_{(0)}$ (–0.4221) of P-PTG faults is less than $-\varepsilon_4$, verifying that the faulty pole can be correctly identified.

6.4.2. Results and discussion of disturbances

As shown in Fig. 13(k) and Fig. 13(l), abrupt changes occur in the $u_{b(1)}$, due to the lightning overvoltage or the operation overvoltage,

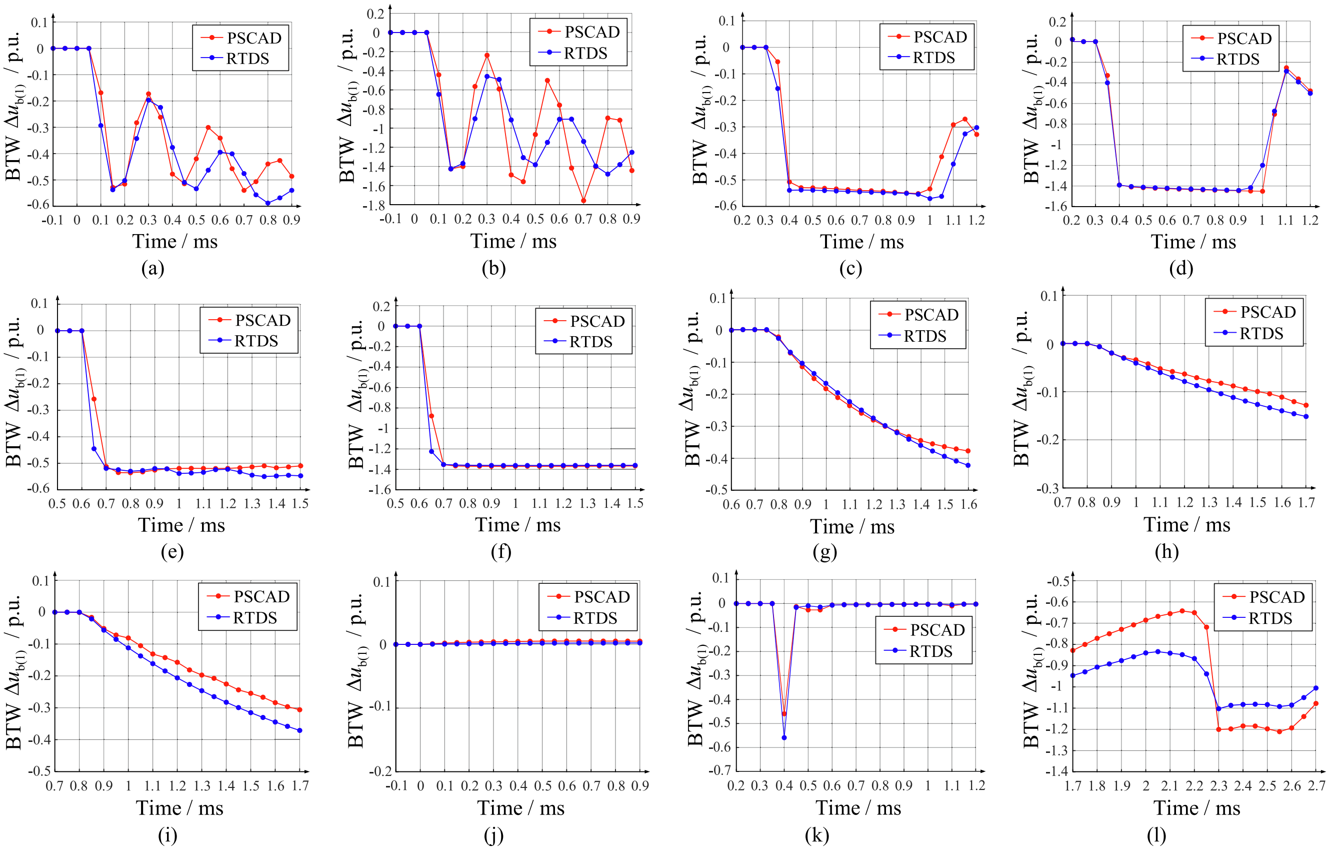

Fig. 13. The simulation results of the backward traveling waves under different short-circuit faults and disturbances. (a) Close internal P-PTG fault F1 (10 %); (b) Close internal PTP fault F1 (10 %); (c) Internal P-PTG fault F1 occurring at the midpoint (50 %); (d) Internal PTP fault F1 occurring at the midpoint (50 %); (e) Remote internal P-PTG fault F1 (90 %); (f) Remote internal PTP fault F1 (90 %); (g) External P-PTG fault F2; (h) Close external P-PTG fault F3 (10 %); (i) Close external PTP fault F3 (10 %); (j) External P-PTG fault F4; (k) Lightning disturbance; (l) Operation disturbance.

Table 3
Results of short-circuit faults.

Fault Type	Fault Pole	Fault Distance/%	$\lg\kappa_{b(1)}$ / p.u.	*RFTR* / p.u.	intg_$i_{(1)}$ / p.u.·ms	intg_$u_{(0)}$ / p.u.·ms	intg_$u_{(1)}$ / p.u.·ms	Identification Result
F1	P-PTG	10	2.1461	∞	0.0047	−0.4221	−0.2687	Internal Fault (P-PTG)
		30	1.7894	∞	0.0061	−0.4782	−0.3196	Internal Fault (P-PTG)
		50	1.3440	∞	0.0073	−0.5365	−0.3736	Internal Fault (P-PTG)
		70	1.2205	∞	0.0052	−0.4856	−0.3983	Internal Fault (P-PTG)
		90	1.1348	∞	0.0025	−0.4430	−0.4144	Internal Fault (P-PTG)
	PTP	10	1.9193	∞	0.0036	0.0000	−0.6719	Internal Fault (PTP)
		30	1.5069	∞	0.0089	0.0000	−0.8277	Internal Fault (PTP)
		50	1.1616	∞	0.0196	0.0000	−1.0379	Internal Fault (PTP)
		70	1.0584	∞	0.0152	0.0000	−1.0439	Internal Fault (PTP)
		90	0.9545	∞	0.0106	0.0000	−1.0528	Internal Fault (PTP)
F2	P-PTG	/	−1.1118	/	/	/	/	External Fault
F3	P-PTG	10	−1.8210	/	/	/	/	External Fault
		50	−2.0757	/	/	/	/	External Fault
		90	−2.4708	/	/	/	/	External Fault
	PTP	10	−1.8996	/	/	/	/	External Fault
		50	−2.2392	/	/	/	/	External Fault
		90	−2.8027	/	/	/	/	External Fault
F4	P-PTG	/	−2.8861	/	/	/	/	External Fault

Table 4
Results of disturbances.

Disturbance Type		$\lg\kappa_{b(1)}$ / p.u.	*RFTR* / p.u.	intg_$i_{(1)}$ / p.u.·ms	intg_$u_{(0)}$ / p.u.·ms	intg_$u_{(1)}$ / p.u.·ms	Identification Result
Lightning Overvoltage	Back-flash without Flashover	3.5285	0.2500	/	/	/	Lightning Disturbance
	Shielding Failure without Flashover (P)	3.2365	0.6667	/	/	/	Lightning Disturbance
Operation Overvoltage	Sending-Terminal DCCB Operation (P)	3.3193	∞	0.6120	/	/	Operation Disturbance
	Receiving-Terminal DCCB Operation (P)	3.1524	∞	0.1414	/	/	Operation Disturbance

which lead to $\lg\kappa_{b(1)}$ (minimum is 3.1524) far exceeding ε_1. Yet, results in Table 4 indicate that, although the $\lg\kappa_{b(1)}$ of disturbances satisfy (29), the *RFTRs* (maximum is 0.6667) are below ε_2 when lightning overvoltage disturbances occur and the intg_$i_{(1)}$ (minimum is 0.1414) are above ε_3 when operation overvoltage disturbances occur. Hence, the supplementary disturbance identification criterion can avoid the protection from being mis-triggered.

6.5. Robustness analysis

The robustness of the protection method is analyzed, when different parameters are changed and noise is added. Due to the space limitation, only the curvatures $\lg\kappa_{b(1)}$ during F1 and F2 (the worst-case scenario of external faults) are provided. The following change range of each parameter refers to the industrial requirement.

6.5.1. Robustness against transition resistance

When transition resistance R_f changes from 0 to 800 Ω, the results of P-PTG faults and PTP faults are shown in Fig. 14. Z-axis represents $\lg\kappa_{b(1)}$, X-axis represents l, and Y-axis represents R_f.

It can be seen from Fig. 14, $\kappa_{b(1)}$ of F1 and F2 both increase with R_f when other parameters are the same, which is consistent with the analysis conclusion in Section 4.4. For the l and R_f verified, the minimum $\lg\kappa_{b(1)}$ of F1 are 1.1348 (P-PTG faults, 0 Ω) and 0.9545 (PTP faults, 0 Ω), when F1 occurs at the far end of Line$_{MN}$. Yet, the maximum $\lg\kappa_{b(1)}$ of F2 is −1.0336, which is much less than ε_1. The results indicate that the curvature-based criterion can correctly identify faults even with the R_f of 800 Ω, proving that its robustness against transition resistance is strong.

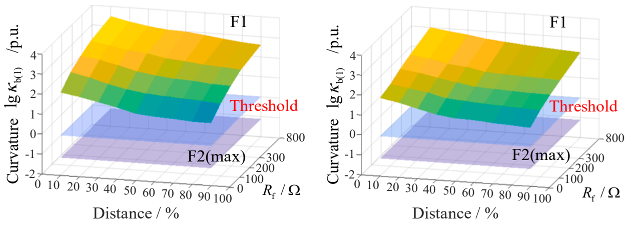

(a) (b)

Fig. 14. Results of different transition resistances. (a) P-PTG; (b) PTP.

6.5.2. Robustness against sampling frequency

When the sampling frequency F_s changes to 10 kHz, 20 kHz, and 50 kHz, the results are shown in Fig. 15. The vertical axis represents $\lg\kappa_{b(1)}$, the horizontal axis represents l, and the numbers in the legend represent F_s.

It can be seen from Fig. 15, F_s has a noticeable influence on $\kappa_{b(1)}$, especially when F_s is low, whereas the influence gradually becomes weak as F_s increases. Yet, as long as F_s satisfies (41), the step-wave characteristics of $u_{b(1)}$ can be sampled, then the $\lg\kappa_{b(1)}$ of F1 far exceed ε_1. For the F_s verified, the minimum $\lg\kappa_{b(1)}$ of F1 are 1.1348 (P-PTG faults, 20 kHz) and 0.9545 (PTP faults, 20 kHz), when F1 occurs at the far end of Line$_{MN}$. Yet, the maximum $\lg\kappa_{b(1)}$ of F2 is −0.4262, which is less than ε_1. The results indicate that the curvature-based criterion can

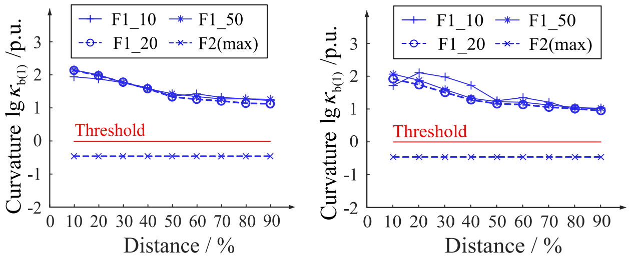

(a) (b)

Fig. 15. Results of different sampling frequencies. (a) P-PTG; (b) PTP.

correctly identify faults even with the F_s of 10 kHz, proving that its robustness against sampling frequency is strong.

6.5.3. *Robustness against current limiting reactor*

When the values of CLR change to 50 mH, 100 mH, 200 mH, and 300 mH, the results are shown in Fig. 16. The vertical axis represents $\lg\kappa_{\mathrm{b}(1)}$, the horizontal axis represents l, and the numbers in the legend represent the values of CLR.

It can be seen from Fig. 16, the $\lg\kappa_{\mathrm{b}(1)}$ of F1 and F2 are hardly affected by CLR. The reason for this phenomenon can be explained as: For F1, the $u_{\mathrm{b}(1)}$ does not pass through the line boundary, so its $\kappa_{\mathrm{b}(1)}$ is not affected by CLR, according to (27); For F2, the $u_{\mathrm{b}(1)}$ passes through the line boundary, but since its $\kappa_{\mathrm{b}(1)}$ is extremely small, the effect coming from the value of CLR can be ignored. For the values of CLR verified, the minimum $\lg\kappa_{\mathrm{b}(1)}$ of F1 are 1.0492 (P-PTG faults, 50 mH) and 0.9175 (PTP faults, 100 mH), when F1 occurs at the far end of Line$_{\mathrm{MN}}$. Yet, the maximum $\lg\kappa_{\mathrm{b}(1)}$ of F2 is -0.5738, which is less than ε_1. The results indicate that the curvature-based criterion can correctly identify faults even with the CLR of 50 mH, proving that its robustness against the values of CLR is strong.

6.5.4. *Robustness against noise*

When white noise, which is commonly chosen for methods verification due to its uniformly distributed power spectral density [35], is added with a signal-to-noise ratio (SNR) of 35 dB, the results are shown in Fig. 17. The vertical axis represents $\lg\kappa_{\mathrm{b}(1)}$, the horizontal axis represents l, and the numbers in the legend represent SNR (the original signals do not have SNR).

It can be seen from Fig. 17, when l is short, noise has an observable effect on the $\kappa_{\mathrm{b}(1)}$ of internal faults. Yet, the noise mainly affects the amplitude of $u_{\mathrm{b}(1)}$, rather than their waveform characteristics, on which the curvature-based method relies. The minimum $\lg\kappa_{\mathrm{b}(1)}$ of F1 are 1.1348 (P-PTG faults, without noise) and 0.8691 (PTP faults, with noise), when F1 occurs at the far end of Line$_{\mathrm{MN}}$. Yet, the maximum $\lg\kappa_{\mathrm{b}(1)}$ of F2 is -0.2407, which is less than ε_1. The results indicate that the curvature-based criterion can correctly identify faults even with a noise of 35 dB, proving that its robustness against noise is strong.

6.5.5. *Robustness against line length*

When line length L changes to 50 km, 200 km, and 1000 km, the results are shown in Fig. 18. The vertical axis represents $\lg\kappa_{\mathrm{b}(1)}$, the horizontal axis represents l, and the numbers in the legend represent the length of lines.

As shown in Fig. 18, it is the fault distance l, not the line length L, that has a noticeable influence on $\lg\kappa_{\mathrm{b}(1)}$ of F1, as analyzed according to (27). The minimum $\lg\kappa_{\mathrm{b}(1)}$ are 0.8741 (P-PTG faults, 1000 km) and 0.7713 (PTP faults, 1000 km), when F1 occurs at the far end of Line$_{\mathrm{MN}}$. Yet, the maximum $\lg\kappa_{\mathrm{b}(1)}$ of F2 is -0.7138, which is less than ε_1. The results indicate that the curvature-based criterion can correctly identify faults even with different L, proving that its robustness against line length is strong.

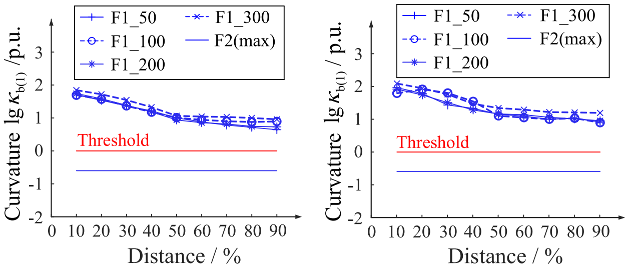

(a)

(b)

Fig. 16. Results of different CLR values. (a) P-PTG; (b) PTP.

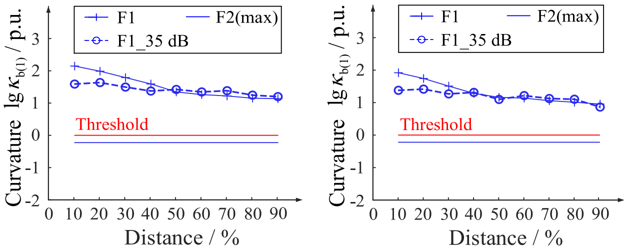

(a)

(b)

Fig. 17. Results with noise. (a) P-PTG; (b) PTP.

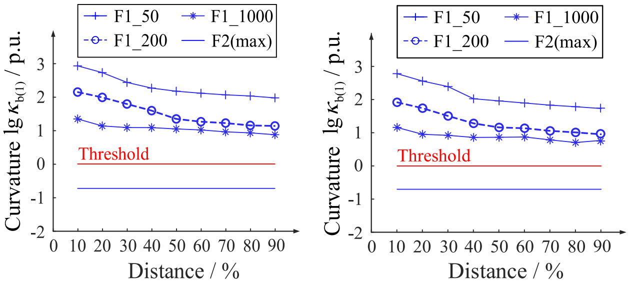

(a)

(b)

Fig. 18. Results of different line lengths. (a) P-PTG; (b) PTP.

6.5.6. *Robustness against system topology and line type*

A transmission line is added between converter stations M and Q, thereby changing the system topology. Besides, the new Line$_{\mathrm{MQ}}$ uses cables for transmission, with a length of 300 km. For protection R$_{\mathrm{MQp}}$, the results are shown in Fig. 19. The vertical axis represents $\lg\kappa_{\mathrm{b}(1)}$, the horizontal axis represents l, and the numbers in the legend represent R_{f}.

It can be seen from Fig. 19, when system topology and line type change, the influence of l and R_{f} on $\lg\kappa_{\mathrm{b}(1)}$ is still consistent with the analysis in Section 4.4. Due to that the line propagation characteristics of cables are severer than those of overhead lines, the abrupt change of $u_{\mathrm{b}(1)}$ is further weakened, leading to smaller $\lg\kappa_{\mathrm{b}(1)}$. Nevertheless, the step-waveform characteristics of $u_{\mathrm{b}(1)}$, on which the curvature-based method relies, can still be sampled in cables. The minimum $\lg\kappa_{\mathrm{b}(1)}$ of F1 are 0.6143 (P-PTG faults, 0 Ω) and 0.5280 (PTP faults, 0 Ω), when F1 occurs at the far end of Line$_{\mathrm{MN}}$. Yet, the maximum $\lg\kappa_{\mathrm{b}(1)}$ of F2 is -1.5272, which is much less than ε_1. The results indicate that the curvature-based criterion can correctly identify faults even with different system topology and line type, proving that its robustness is strong.

6.6. *Comparison study*

6.6.1. *Parameter comparison*

The proposed method is compared with the existing methods based

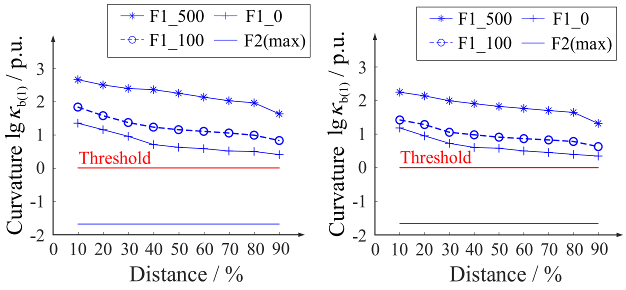

(a)

(b)

Fig. 19. Results of different system topology and line type. (a) P-PTG; (b) PTP.

Table 5
Parameter comparison of different methods.

Method	Type	Sampling Frequency	Resistance Robustness	Detection Time
Proposed Method	Non-unit	10 kHz	800 Ω	1 ms
Change Rate (ROCOV) [19]	Non-unit	100 kHz	200 Ω	1 ms
Ratio (ROTV) [20]	Non-unit	10 kHz	400 Ω	1 ms
Variation ($\Delta u_{b(1)}$) [21]	Non-unit	100 kHz	200 Ω	1 ms
Integration (Eu_b) [22]	Non-unit	10 kHz	200 Ω	1 ms
Correlation [23]	Unit	1 MHz	300 Ω	1 ms
Direction [24]	Unit	250 kHz	400 Ω	2 ms

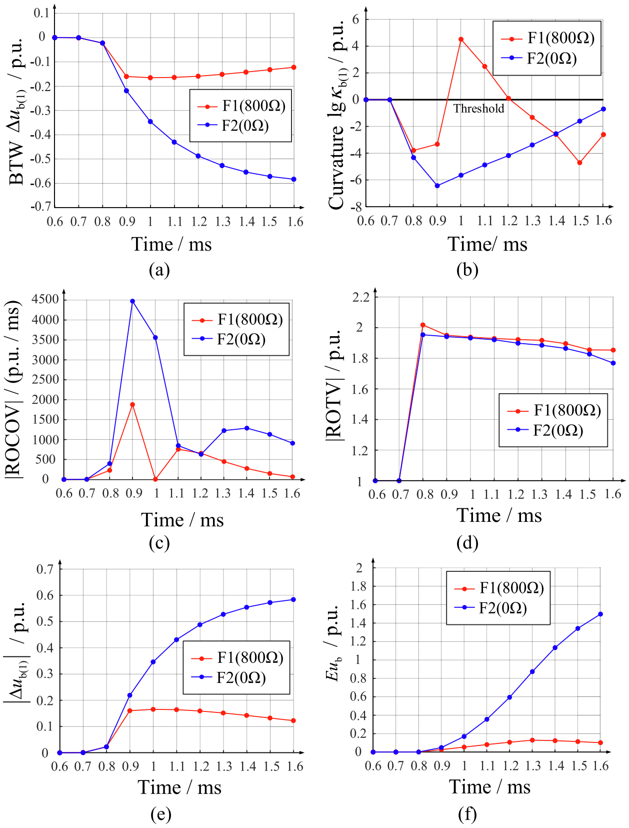

(a) (b) (c) (d) (e) (f)

Fig. 20. Results of simulation verification. (a) 1-mode backward traveling waves; (b) The logarithm of the curvatures of 1-mode backward traveling waves; (c) The absolute value of ROCOV; (d) The absolute value of ROTV; (e) The absolute value of the variation of 1-mode backward traveling waves; (f) The energy of backward traveling waves.

on time-domain traveling wave characteristics, which are reviewed in Section 1. The results are shown in Table 5, and the parameters include the protection type, the sampling frequency, the robustness against resistance, and the detection time. It should be noted that the detection time refers to the period from fault traveling waves arriving at the protection device to the protection device outputting identification results. In addition, the values of the sampling frequency, the robustness of resistance, and the detection time come from simulation results or experimental results of the existing methods reviewed in Section 1.

ROCOV represents the rate of change of voltage, ROTV represents the ratio of transient voltage, $\Delta u_{b(1)}$ represents the variation of 1-mode backward traveling waves, and Eu_b represents the energy of backward traveling waves. As Table 5 shows, the proposed curvatures-based method can improve the robustness against resistance. Besides, its short detection time and low sampling frequency can reduce the investment for equipment and meet the requirements of MMC-HVDC grids.

6.6.2. Simulation verification

The existing non-unit methods listed in Table 5 are verified under extreme conditions, and are compared with the proposed method. Fault types are remote internal high-resistance P-PTG fault (F1) occurring at 100 % of Line$_{MN}$, and external metallic P-PTG fault (F2) occurring at Bus N. The sampling frequency is 10 kHz, the data window is 1 ms, the value of CLR is 50 mH, the transition resistance (only for F1) is 800 Ω, and the start time is 0 ms. The simulation and verification results are shown in Fig. 20.

As shown in Fig. 20(a), in the abovementioned extreme scenario, the amplitude of the $u_{b(1)}$ when F2 occurs far exceeds that of F1. Yet, the step-wave characteristics of $u_{b(1)}$ can still be sampled when F1 occurs, hence, the curvature-based method can correctly identify F1 from F2, even under the extreme condition, as shown in Fig. 20(b). However, the other compared methods may misidentify faults, because the characteristics of F2 are close to F1 (ROTV) or more noticeable than F1 (ROCOV, $\Delta u_{b(1)}$, and Eu_b), as shown in Fig. 20(c) to Fig. 20 (f), hence, it is hard to set thresholds. The comparison shows that the proposed method has low requirements for sampling frequency, data window, and CLR value, and has strong robustness against transition resistance.

7. Conclusion

A non-unit protection method based on the curvatures of backward traveling waves for MMC-HVDC grids is proposed, theoretical analysis and simulation verification show that:

(1) When an internal fault occurs, the backward traveling waves received by the protection device appear as obvious step waves and drop rapidly. When an external fault occurs, the backward traveling waves drop smoothly and continuously.
(2) The curvatures can clearly distinguish internal faults and external faults based on the backward traveling wave characteristics, and can be used to construct a non-unit protection method.
(3) The protection method for MMC-HVDC grids can correctly identify faults under different transition resistances and fault distances, and has the advantages of low sampling frequency requirement, strong tolerance against transition resistance and noise, insensitivity to line boundary parameters, and no threshold setting reliance on simulation data.

CRediT authorship contribution statement

Fan Xie: Conceptualization, Software, Methodology, Data curation, Investigation, Validation, Writing – original draft, Writing – review & editing. **Zhiguo Hao:** Writing – review & editing. **Dongmeng Ye:** Conceptualization, Methodology. **Songhao Yang:** Writing – review & editing. **Chuanxi Li:** Validation. **Guoan Dai:** Validation. **Baohui Zhang:** Supervision. **Ting Wang:** Funding acquisition, Writing – original draft, Writing – review & editing.

Declaration of Competing Interest

The authors declare that they have no known competing financial interests or personal relationships that could have appeared to influence the work reported in this paper.

Data availability

The authors do not have permission to share data.

Acknowledgments

This work was supported by the National Natural Science Foundation of China (52107124).

References

[1] Geddada N, Yeap YM, Ukil A. Experimental validation of fault identification in VSC-based DC grid system. IEEE Trans Ind Electron Jun. 2018;65(6):4799–809.
[2] Zhang L, et al. Modeling, control, and protection of modular multilevel converter-based multi-terminal HVDC systems: a review. CSEE J Power Energy Syst Dec. 2017;3(4):340–52.
[3] Nami A, Liang J, Dijkhuizen F, Demetriades GD. Modular multilevel converters for HVDC applications: review on converter cells and functionalities. IEEE Trans Power Electron Jan. 2015;30(1):18–36.
[4] Li Z, et al. Accurate impedance modeling and control strategy for improving the stability of DC system in multiterminal MMC-based DC grid. IEEE Trans Power Electron Oct. 2020;35(10):10026–49.
[5] Zhang C, Song G, Dong X. Non-unit ultra-high-speed DC line protection method for HVDC grids using first peak time of voltage. IEEE Trans Power Deliv Jun. 2021;36 (3):1683–93.
[6] Huang Q, Zou G, Zhang S, Gao H. A pilot protection scheme of DC lines for multi-terminal HVDC grid. IEEE Trans Power Deliv Oct. 2019;34(5):1957–66.
[7] Han X, Sima W, Yang M, Li L, Yuan T, Si Y. Transient characteristics underground and short-circuit faults in a ±500 kV MMC-based HVDC system with hybrid DC circuit breakers. IEEE Trans Power Deliv Jun. 2018;33(3):1378–87.
[8] Yang S, Xiang W, Wen J. An improved DC fault protection scheme independent of boundary components for MMC based HVDC grids. IEEE Trans Power Deliv Aug. 2021;36(4):2520–31.
[9] Merlin VL, Dos Santos RC, Le Blond S, Coury DV. Efficient and robust ANN-based method for an improved protection of VSC-HVDC systems. IET Renew Power Gener Jun. 2018;12(13):1555–62.
[10] Baghaee HR, Mlakic D, Nikolovski S, Dragicevic T. Anti-islanding protection of PV-based microgrids consisting of PHEVs using SVMs. IEEE Trans Smart Grid Jan. 2020;11(1):483–500.
[11] Luo G, et al. Stacked auto-encoder-based transients recognition in VSC-HVDC. IEEE Access Jan. 2020;8:14223–33.
[12] Bertho R, Lacerda VA, Monaro RM, Vieira JCM, Coury DV. Selective nonunit protection technique for multiterminal VSC-HVDC grids. IEEE Trans Power Deliv Oct. 2018;33(5):2106–14.
[13] Xiang W, Yang S, Adam GP, Zhang H, Zuo W, Wen J. DC fault protection algorithms of MMC-HVDC grids: fault analysis, methodologies, experimental validations, and future trends. IEEE Trans Power Electron Oct. 2021;36(10): 11245–64.
[14] Silva DM, Costa FB, Franca RLS, Junior FCS. “Wavelet-based detection of transients induced by DC faults using boundary protection principle. In: *2018 IEEE Power & Energy Society General Meeting (PESGM)*, Portland, OR, USA, 2018, pp.1-5.
[15] Ye D, Xie F, Hao Z. “A novel identification scheme of lightning disturbance in HVDC transmission lines based on CEEMD-HHT. CPSS Trans Power Electron Appl 2021;6(2):145–54.
[16] Li B, Li Y, He J, Wen W. A novel single-ended transient-voltage-based protection strategy for flexible DC grid. IEEE Trans Power Deliv Oct. 2019;34(5):1925–37.
[17] Liao J, Zhou N, Wang Q. DC grid protection method based on phase planes of single-end common-and differential-mode components. IEEE Trans Power Deliv Feb. 2021;36(1):299–310.
[18] Sun J, Debnath S, Bloch M, Saeedifard M. A hybrid DC fault primary protection algorithm for multi-terminal HVDC systems. IEEE Trans Power Deliv Apr. 2022;37 (2):1285–94.
[19] Leterme W, Beerten J, Van Hertem D. Nonunit protection of HVDC grids with inductive DC cable termination. IEEE Trans Power Deliv Apr. 2016;31(2):820–8.
[20] Liu J, Tai N, Fan C. Transient-voltage-based protection scheme for DC line faults in the multiterminal VSC-HVDC system. IEEE Trans Power Deliv Jun. 2017;32(3): 1483–94.
[21] Zhang Y, Tai N, Xu B. Fault analysis and traveling-wave protection scheme for bipolar HVDC lines. IEEE Trans Power Deliv Jul. 2012;27(3):1583–91.
[22] Kong F, Hao Z, Zhang S, Zhang B. Development of a novel protection device for bipolar HVDC transmission lines. IEEE Trans Power Deliv Oct. 2014;29(5):2270–8.
[23] Tang L, Dong X, Luo S, Shi S, Wang B. A new differential protection of transmission line based on equivalent travelling wave. IEEE Trans Power Deliv Jun. 2017;32(3): 1359–69.
[24] Wang D, Yu D, Yang H, Hou M, Guo Y. Novel travelling wave directional pilot protection for VSC-HVDC transmission line. IET Gener Transm Distrib May 2020; 14(9):1705–13.
[25] Zhang C, Song G, Dong X. A novel traveling wave protection method for DC transmission lines using current fitting. IEEE Trans Power Deliv Dec. 2020;35(6): 2980–91.
[26] Yu X, Xiao L. A DC fault protection scheme for MMC-HVDC grids using new directional criterion. IEEE Trans Power Deliv Feb. 2021;36(1):441–51.
[27] Wang Y, Xie F, Hao Z. “Analytical method for the initial travelling wave of transmission line faults in VSC-HVDC grid.” In: *2020 Tsinghua-HUST-IET Electrical Engineering Academic Forum*, Beijing, China, 2020, pp.1-7.
[28] Aghamohamadian-Sharbaf M, Pourreza HR, Banaee T. A novel curvatures-based algorithm for automatic grading of retinal blood vessel tortuosity. IEEE J Biomed Heal Inform Mar. 2016;20(2):586–95.
[29] Liu D, Duan J, Shi H. A strong tracking square root central difference FastSLAM for unmanned intelligent vehicle with adaptive partial systematic resampling. IEEE Trans Intel Transp Sys Nov. 2016;17(11):3110–20.
[30] Xie F, Hao Z, Ye D, Zhang B, Liu Z. “A RFTR based lightning disturbance identification scheme for VSC-HVDC line protection. In: *Tsinghua University-IET Electrical Engineering Academic Forum: Constructing Green and Sustainable Energy System (2021)*, vol. 2021, 2021, pp. 75–80.
[31] Wang T, Yu Z, Xie F, Hao Z, Monti A, Ponci F. Protection of line faults in HVDC grids through convexity detection in backward traveling wave voltages. IEEE Trans Power Deliv, early access.
[32] Tay TT, Mareels IMY, Moore JB. “Off-line controller design”, in “*High Performance Control*” (Birkhäuser, 1998, 1st edn.), pp. 92–95.
[33] Elimban S, Zhang Y, Garcia Alonso JC. “Real time simulation for HVDC grids with modular multi-level converters,” In: 11th IET International Conference on AC and DC Power Transmission, Birmingham, 2015, pp. 1-8.
[34] Fan X, Wang Y, Zang B. Fast electromagnetic transient simulation for flexible DC power grid. Autom Electric Power Syst Feb. 2017;41(4):92–7.
[35] Zhivomirov H. A method for colored noise generation. Roman J Acoust Vib Jan. 2018;15(1):14–9.